

Programmable Multistable Perforated Shellular

Jiahao Shi, Hossein Mofatteh, Armin Mirabolghasemi, Gilles Desharnais, and Abdolhamid Akbarzadeh*

Developing bistable metamaterials has recently offered a new design paradigm for deployable structures and reusable dampers. While most bistable mechanisms possess inclined/curved struts, a new 3D multistable shellular metamaterial is developed by introducing delicate perforations on the surface of Schwarz's Primitive shellular, integrating the unique properties of shellular materials such as high surface area, stiffness, and energy absorption with the multistability concept. Denoting the fundamental snapping part by motif, certain shellular motifs with elliptical perforations exhibit mechanical bistability. To bring the concept of multistability to a single motif, multistable shellular motifs are developed by introducing multilayer staggered perforations that form hinges and facilitate local instability. Adopting an n -layer staggered perforation (n hinges) design leads to a maximum 2^{n-1} stable states within one shellular motif during loading and unloading. Three-directional multistable shellulars are attained by extending the perforation design in three orthogonal directions. Harnessing snap-through and snap-back behaviors and self-contact, the introduced multistable perforated shellulars exhibit strong rigidity both in loading and unloading, and enhanced energy dissipation. The introduced design strategy opens up new horizons for creating multidirectional multistable metamaterials with load bearing capabilities for applications in soft robotics, shape-morphing architectures, and reusable and deployable energy absorbers/dampers.

from their underlying rationally-designed architectures rather than the intrinsic attributes of their constitutive materials. Tailoring multiphysical properties of metamaterials and making them adaptable to the constantly changing requirements of real-life applications as multifunctional materials, demand for programmability. Utilizing reconfigurable mechanical metamaterials can offer a reliable solution to render programmable properties, such as tunable acoustic^[7,8] and photonic^[9,10] bandgaps, for performance tuning of advanced materials on demand. Structural multistability enables achieving large deformation by harnessing elastic instability and retaining different stable configurations without an external load.^[11] Additionally, with recent advances in 3D/4D printing, structural multistability provides a new pathway for shape reconfiguration,^[12,13] shock isolation,^[11,14] reusable energy absorption,^[11,15,16] and rapid response actuation.^[17–19] Therefore, developing next generation of multistable mechanisms imparts new routes for programming multifunctional and adaptive architected metamaterials.

1. Introduction

As a class of artificial materials, metamaterials exhibit unprecedented properties that are hardly found in current naturally occurring materials (e.g., negative refractive index,^[1,2] negative incremental stiffness,^[3,4] negative Poisson's ratio,^[4,5] and apparent negative thermal conductivity^[6]), mainly emanated

Featuring two structurally stable states, bistable mechanical metamaterials are marked by their unique local minima of the elastic potential energy and exhibit snap-through/back behaviors with negative incremental stiffness. Most of these rationally-designed materials are comprised of two pivotal elements, that is, constrained inclined^[11] or curved^[20] beams and 3D shallow domes.^[21] Structural multistability can be realized by assembling these bistable elements in a form of 1D chains,^[22] 2D planar/cylindrical sheets,^[11,22,23] or 3D lattices.^[11,22,24] By tailoring the topology of their underlying architectures, a series of multiphysical properties (e.g., elastic waves bandgaps,^[25] strain energy entrapment,^[11] thermal expansion coefficient, and Poisson's ratio^[23]) of the bi-/multistable metamaterials can be tuned. Rapid shape-changing triggered by external stimuli (e.g., water or solvent content^[19] and temperature change^[26]) is viably realized in mechanical metamaterials fabricated by passive constitutive solids. Several design strategies for structural bi-/multistability, including but not limited to creased cones,^[14] foldable origamis,^[27] waved sleeves,^[28] compliant hinges,^[12,27] multiple magnetic system,^[29] and integrated granular particles and compliant stretchable components,^[30] have been proposed for developing deployable structures with improved stiffness

J. Shi, H. Mofatteh, A. Mirabolghasemi, A. H. Akbarzadeh
Department of Bioresource Engineering
McGill University
Montreal QC H9X 3V9, Canada
E-mail: hamid.akbarzadeh@mcgill.ca

G. Desharnais
Axis Prototypes
Montreal QC H1P 3C1, Canada

A. H. Akbarzadeh
Department of Mechanical Engineering
McGill University
Montreal QC H3A 0C3, Canada

 The ORCID identification number(s) for the author(s) of this article can be found under <https://doi.org/10.1002/adma.202102423>.

DOI: 10.1002/adma.202102423

and durability. The motifs or building blocks of these metamaterials (i.e., the fundamental region of the cell, which has more than one stable state and from which the whole architecture can be built using various transformations) switch only between two stable configurations and multistability is commonly achieved by utilizing an assembly of these bistable blocks. Exploiting 3D motifs with arbitrary stable configurations facilitates the realization of the redeployable structures with multiple configurations and soft robots with a plethora of controllable displacement degrees of freedom. see [29]

Due to their highly nonlinear deformation behavior caused by their intriguing structural instability, elastic shells can be invoked to design multistable unit cells for mechanical metamaterials that can adapt themselves to loading conditions.^[31]

Conventional bistable or tristable shells (e.g., half tennis ball^[32] and Venus flytrap^[33]) display buckling^[18] and snapping^[34] configurations, determined by their curvature, prestress, and residual stress.^[31] In addition, surface patterning, like corrugation,^[35] or varied thickness surfaces,^[34] can impose structural multistability in elastic shells. Based on polyhedron templates and high degrees of freedom of soft hinges, assembled prismatic metamaterials can exhibit multistable behavior along multiple directions;^[36] nevertheless, to the best of the authors knowledge, none of the existing polyhedron-based multidirectional multistable cells can achieve the stable states independently along different directions, as their multidirectional stable states are not independent of each other, and the realization of a new stable state in one direction can break the multistability in other directions.

As a new type of architected materials, shell-based cellular solids or “shellulars” (as a portmanteau word blending “shell” and “cellular”) are composed of periodic 3D unit cells of continuously smooth and curved thin shells.^[37] With less sensitivity to stress concentration and architectural defects than truss and plate-based cellular solids, shell-like metamaterials have shown promising potentials for achieving enhanced stiffness and strength,^[37–39] and extreme resilience^[40] at ultralow relative density. While shellular metamaterials can be formed by any non-self-intersecting shell surface, they are often developed based on triply periodic minimal surfaces (TPMS), for example, Schwarz P (Primitive), Schwarz D (Diamond), and Gyroid, in which, “triply periodic” refers to periodicity in three directions and “minimal surfaces” represents a locally minimum surface area for a given boundary.^[41] TPMSs are intersection-free smooth surfaces with zero mean curvature at any point and they partition the space into two independent but intertwined continuous sub-volumes.^[41] The geometric features of TMPS hold great promise for creating shellular materials with unrivaled multifunctional properties, such as minimal stress concentration, high fluid permeability, and enhanced heat transfer, for a wide range of applications in bionic scaffold,^[42,43] catalytic converters,^[44] heat exchanger,^[45] ultrafiltration,^[46] and microbatteries.^[47] Although the rapid snapping and fast closure of Venus flytrap^[48] in the nature exemplifies the bistability of shell-like architectures, structural bi-/multistability of shellulars with complex architectures are yet to be discovered. This study presents a novel design and manufacturing route for realization of programmable and previously inaccessible deployable multi-stable perforated shellulars that can unveil desired number of

stable states in their motifs, from monostable to multistable, supported by experiments demonstrating multistable cells with quadstable motifs.

In this research, we implement the multistable design concept on the Schwarz’s Primitive (P) surface through exploiting two perforation strategies: 1) Vertical elliptical holes (as bistability pattern) and 2) Staggered horizontal rectangular holes (as multistability pattern). Samples of bi-/multistable cells and their motifs are presented in Figure S1, Supporting information. By engineering the geometrical parameters of the P shellular and the selected perforation profiles, we demonstrate how bistability can be achieved in P shellular motifs with elliptical holes, while the staggered perforation can lead to bi-/tri-/quad-/multistable motifs. Numerical simulation, theoretical spring modeling, and mechanical testing are conducted to confirm the structural multistability of the introduced perforated P shellular metamaterials. Furthermore, the perforated motifs are employed to design and manufacture 3D unit cells that exhibit decoupled shape reconfigurations and multistable load-bearing states, under both tension and compression, along three distinct orthogonal directions. The introduced design framework offers a new paradigm for realization of reconfigurable advanced materials in the form of programmable shell-based multistable mechanical metamaterials for potential applications as soft robotic grippers/muscles, actuators, reusable energy absorbers, and adaptive structures.

2. Results and Discussion

The unit cells of bistable perforated shellular metamaterials are designed by adding perforations through P shellulars. Mathematically, the P shellular mid-surface is defined by $\cos(x) + \cos(y) + \cos(z) = f$, where f is level set constant that varies from 0 to 1.^[49] The proposed bistable mechanism in this study finds inspiration from the bistability of a spherical cap, similar to the shell surface eversion of an umbrella in a strong gust of wind or a contact lens when being inside-out. The unit cells of designed perforated P shellular metamaterials, as a family of thin shells and inclined beams, can exhibit a bistable behavior with symmetrically deformed perforated segments under compression applied on their top surface (marked by orange color); fixed boundary conditions are assigned to the four side surfaces (indicated by red color) (**Figure 1a**). Negative incremental stiffness is observed in the representative compressive stress-strain curves for both intact (Figure 1b) and perforated (Figure 1c) half-cells when a compressive force reaches F_{\max} . While loading, the intact shellular part merely presents a positive noninitial minimum force $F_{\min} > 0$ and upon unloading, it returns to its original stable state (state i in Figure 1b), demonstrating a monostable snap-through behavior. In Figure 1c, the half-cell of perforated shellular, in contrast, restores the state iii and holds two stable states (states i and iii) and exhibits bistable behavior. Detailed explanation on the structural stability criteria for determining the bistable mechanical metamaterials is given in Figure S2, Supporting Information. In the following analyses, we use the ratio of E_{out} due to the second stable configuration, and E_{snap} , energy required for material instability in the unloading and

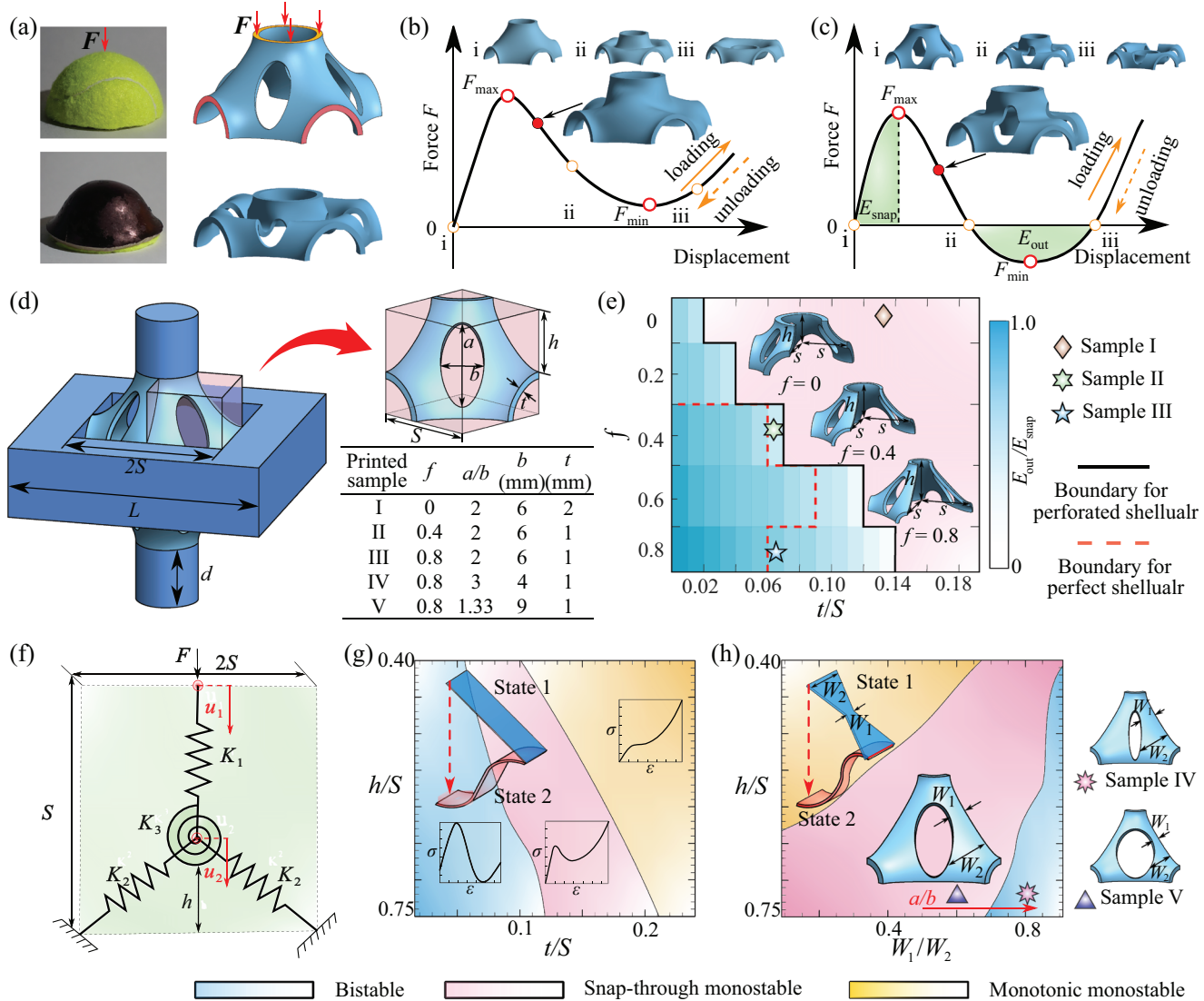


Figure 1. Overview of bistable P shellular motif. a) The designed half-cell of perforated P shellular metamaterial can exhibit two stable states, when four sides (marked by red color) are fixed and the pressure is applied on the top surface (highlighted by the orange color). b,c) Force–displacement curve of half-cell of intact P shellular with $f=0$ shows snap-through behavior while the perforated counterpart can present mechanical bistability, indicated by the sign of their reaction force F . d) Geometrical parameters of the designed perforated P shellular unit cells. Five samples with different level set constants f , perforation size a and b , and thickness t are 3D printed by SLS. e) The effect of level set f and shell thickness t/S on the bistability of perforated (with $a/b=2$ and $b/S=0.4$) and intact shellulars, investigated by FE simulation. The blue color shade only applies to the perforated shellulars. f) Spring model for the theoretical analysis of perforated shellulars. g,h) Phase diagrams for the mechanical response of spring model under uniaxial compression in the parameter space (h/S , t/S) and (h/S , W_1/W_2) showing monotonic monostable, snap-through monostable, and bistable region. $t/S=1/15$ in (h).

loading, respectively, to assess the structural bistability of perforated shellular unit cells and to evaluate their potentials for absorbing and trapping energy.

Figure 1d shows our perforated shellular unit cell, where a solid frame is used to fix the displacement of shell sides and the two cylindrical bars at the top and bottom limit the local shell deformation. The elliptical holes are located in the center of eight evenly divided shellular segments and their longer axes lie on $y=\pm x$ planes, along the cylindrical bars. To evaluate the relationship between geometrical parameters and structural bistability, five samples with three replicates and alternative level set constants (f), ellipse sizes (a and b), and surface

thickness (t) are 3D printed by selective laser sintering (SLS) out of thermoplastic polyurethane (TPU). The unit cell size is $5\text{ cm} \times 5\text{ cm} \times 5\text{ cm}$ with frame length L , as 5 cm , shellular size $2S$, as 3 cm , and cylinder bar height d , as 1 cm . Details on SLS 3D printing and associate material properties of TPU are provided in Figures S3 and S4, Supporting information. While the viscoelasticity of TPU causes energy dissipation through the rate-dependent deformation and the rate-independent snap-back, the bi-/multistability of our rationally-designed perforated shellulars is not originated by the viscoelastic energy dissipation of the parent material (Figures S5 and S6, Supporting Information), since the stable states are defined based on the

quasi-static response of the designed architectures, requiring sufficient resting time for the base material to reach steady-state equilibrium.

The influence of level set constant f and relative thickness t/S on the response of perforated shellular unit cells under uniaxial compression is also investigated by finite element (FE) simulation under a quasi-static condition (Figures S7–S9, Supporting information). As reflected in Figure 1e, snap-through and bistable behaviors of the half-cells of the designed metamaterials highly depend on the assessed architectural parameters. In specific, increasing the level set constant f or decreasing relative thickness t/S , leads to stronger bistability, indicated by a phase transition boundary (solid black line) and a high $E_{\text{out}}/E_{\text{snap}}$ (darker blue areas). For example, for a small level set constant and a high relative thickness ($f = 0$, $t/S = 2/15$), both numerical and experimental results approve the monostable snap-through behavior for sample I, while samples II ($f = 0.4$, $t/S = 1/15$) and III ($f = 0.8$, $t/S = 1/15$) present bistable behavior with energy trapping capabilities. Although we have observed a bistable domain for the half-cell of intact P shellulars (enclosed by dashed red lines in Figure 1e), introducing perforations on the P shellular remarkably expands the bistable region, offering bistability for a wider range of f from 0 to 0.8. The smaller bistability region for the intact shellular might be due to its relatively higher circumferential stiffness; the constrained circumferential expansion under compression can lead to shell wrinkling that prevents symmetrical deformation and results in a global buckling of the shellular.

To better understand the underlying mechanics of the observed mechanical behaviors in the experiments and FE simulations, a theoretical model of a half-cell consisting of pin jointed compressive (K_1 and K_2) and torsional (K_3) springs are developed (Figure 1f). As a simplification of the motif of the designed shell-based unit cell in Figure 1d, K_1 spring stands for the rigid cylindrical bar with stiffness assumed as infinite compared to the compliant shellular; the displacement of flexible segments is divided into bending and compression components, represented by torsional (K_3) and compressive (K_2) springs respectively. Therefore, counteraction between K_2 and K_3 springs determines the bistability of perforated shellulars. As depicted in Figure 1f, the sign of the reaction moment from K_3 spring (i.e., the bending moment of the shell) remains unchanged under compression, making it serve as a recovering force that always pushes the perforated unit cell to retain its initial state. On the contrary, the sign of reaction force direction of K_2 spring varies during the deformation; when displacement u_2 is beyond h , the opposite direction of reaction force from K_2 springs along the vertical displacement provides a possibility to achieve new stable states. In extreme cases of ultrathin shellulars with negligible bending stiffness K_3 , the spring system always holds two stable configurations at $u_2 = 0$ and $u_2 = 2h$.

By simplifying the curved perforated shellulars with an inclined straight plate and determining its corresponding stiffness K_2 and K_3 (assuming an infinite stiffness for K_1) in Figure 1f, we can distinguish three different mechanical behaviors, that is, bistable, snap-through monostable, and monotonic monostable, based on different combinations of h/S and t/S . As provided in section S6 of Supporting information, since K_2 spring stiffness shows a linear relationship with

shell's thickness (t) and K_3 spring stiffness has a cubic relationship, increasing the shellular thickness has more considerable influence on K_3 spring than K_2 . Therefore, decreasing t/S transforms the response of the perforated shellular motif from a monotonic or snap-through monostable to a bistable one. Meanwhile, higher h/S (corresponding to larger level set value f) creates longer shell segments between the perforations, which has no effect on their simplified compressive stiffness K_2 and it only reduces their bending stiffness K_3 , increasing the magnitude of the maximum negative force and resulting in higher energy trapping through the bistable behavior. Since increasing f leads to a higher h/S (as shown by the representative half-cell of shellulars with different f in Figure 1e), the proposed spring model well explains the trends found in Figure 1e, where a smaller t/S or a higher h/S is desirable in the bistable region. In order to better elicit the effect of elliptical perforation shapes on the mechanical behavior, Figure 1h uses an inclined trapezoidal plate (instead of the previously assumed rectangular shape in Figure 1g), to represent the perforated shellulars. The model shows that a higher a/b or a smaller W_1/W_2 is desirable for bistable architectures, a conclusion that has been validated by conducting experiments on 3D printed samples IV and V. The stiffness K_2 and K_3 of the straight and trapezoidal plates in the presented simplified model are related to the geometrical features of shellular segments as explained in Figures S10 and S11, Supporting information.

Figures 2a,b show the stress-strain curves and deformation modes of the 3D printed samples I and III through experimentation and FE simulation. Two noninitial positive local minima for stress during loading indicate the monostable snap-through behavior of sample I. Meanwhile, sample III demonstrates snap-through and tristable response with three stable states at $\epsilon = 0$, 0.24, and 0.42. The different mechanical responses of the two samples I and III are aligned with the proposed abstract spring model in detecting mechanical bistability. As shown in Figure 1g, increasing h/S or f and decreasing t/S facilitate the bistability of perforated shellulars. The agreement between numerical and experimental results corroborates the accuracy of the numerous FE simulations carried out for preparing Figure 1e. Details on the deformation patterns and stress-strain curves of the other three samples can be found in Figure S12, Supporting information. Additionally, Video S1, Supporting Information, presents their mechanical responses during the uniaxial compression (loading) and tension (unloading) tests.

Although samples I and III in Figure 2a,b deform in a layer-by-layer manner, due to the similarity of topological features of the two layers (top and bottom shell), the deformation sequence is uncertain and is mainly governed by the geometrical imperfections of the 3D printed samples and the boundary conditions imposed by the testing machine's fixture. A heterogeneous design of perforated shellulars, in which the architectural parameters of neighboring motifs are distinct, can overcome the indeterminacy of their deformation sequence, putting forward a design methodology for mechanical metamaterials with controllable configurations. In Figure 2c, a connected pin jointed spring system in series is built to represent the assembly of the perforated shellular units, where $K_e^{(i)}$ represents the effective initial stiffness of i^{th} motif ($i = 1, 2, \dots, 2n$, where n represents the number of unit cells each containing

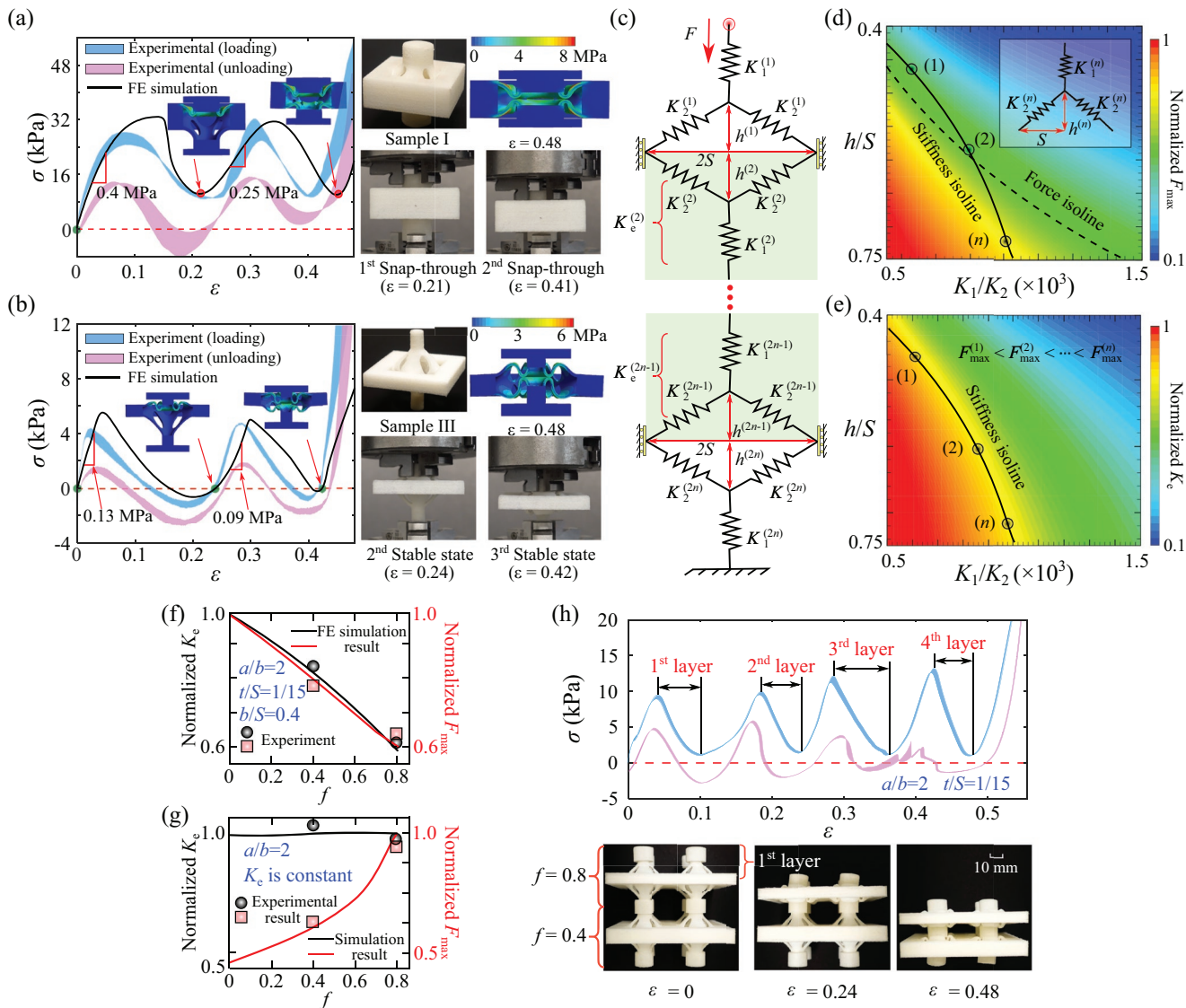


Figure 2. Programmability of bistable perforated P shellulars. a,b) Experimental (blue and pink area) and FE simulation (black solid line) stress-strain curves of samples I and III. c) Spring model for tessellated multilayer perforated shellular. d,e) Contour of normalized snapping force F_{\max} and effective initial stiffness K_e in the parameter space (h/S , K_1/K_2) for a spring subunit, representing a motif of the perforated shellular. f) Influence of f on normalized K_e and F_{\max} of perforated shellular motifs with the same thickness and perforation size. g) Influence of f on normalized F_{\max} with the same K_e and perforation size. h) Experimental results of 3D printed graded perforated shellulars with the same thickness.

2 motifs) of the spring system consisting of $K_1^{(i)}$ and $K_2^{(i)}$ springs. Focusing on thin shells with small bending stiffness, the rotational spring $K_3^{(i)}$, presented in Figure 1f, is neglected in this model. Since under quasi-static deformations, the forces within all subunits are equal to the external force F , motifs with a lower critical/snapping force deform first, indicating that the magnitudes of their F_{\max} determine the deformation sequence of the simplified spring system and its corresponding assembly of bistable units.

Figures 2d,e present the contour of the snapping force F_{\max} and effective initial stiffness K_e (both normalized by their respective maximum values) in the parameter space (h/S , K_1/K_2) for a spring subunit. Even though increasing both h/S and K_1/K_2 leads to smaller normalized F_{\max} and K_e , the two

contour plots show different patterns, that is, positive curvature of force isoline (dashed line in Figure 2d) and negative curvature of effective stiffness isoline (solid line in Figure 2d). Therefore, based on the force isoline, we can program multilayer perforated shellular metamaterials with a desired overall stiffness and deformation sequence (programmable architectural configuration), in which the points in the stiffness isoline satisfy $K_e^{(1)} = K_e^{(2)} = \dots = K_e^{(n)}$ while $F_{\max}^{(1)} < F_{\max}^{(2)} < \dots < F_{\max}^{(n)}$.

An approach for realizing deployable perforated shellular metamaterials and metastructures with deterministic deformation configuration is to vary the level set constant f of the perforated shellular segments of the adjacent unit cells. As shown in Figure 2f, for a given shellular thickness ($t/S = 0.06$) and perforation geometry ($a/b = 2$ and $b/S = 1/15$), both effective

stiffness K_e and snapping force F_{max} exhibit a decreasing trend by increasing the level set constant f . As a result, if we make an assembly of heterogeneous perforated shellular unit cells with the same thickness and hole size but with dissimilar level set constants, the deformation sequence occurs in a reverse order with respect to f value, since $F_{max}(f=0) > F_{max}(f=0.2) > \dots > F_{max}(f=0.8)$. Similarly, for a predefined value of level set constant and perforation size, increasing the shellular thickness leads to a higher effective stiffness and snapping force, and consequently, reconfiguration begins from the thinnest sub-units among the motifs.

As an important material property, constant effective stiffness during shape reconfiguration is desired to realize robust multiphysical properties, such as blocking specific wave propagation in phononic metamaterial.^[50] Figure 2g provides the relationship between snapping force F_{max} and level set f for a perforated shellular motif with a predefined effective stiffness and perforation size, in which F_{max} monotonically increases when f increases. Therefore, in contrast to Figure 2f, the deformation sequence that is directly associated with F_{max} shares the same order with f , that is, among the motifs in series having the same effective initial stiffness K_e and the same perforation size, those with smaller level set constant deform first.

In order to validate the proposed scheme for controlling deformation sequence, perforated shellular samples containing $2 \times 2 \times 2$ cells (three replicate for each design) are designed and 3D printed based on samples II and III (introduced in Figure 1d), and the experimental test results are presented in Figure 2h. Based on the magnitude of maximum snapping force/stress, the deformation sequence of the perforated shellular metamaterial starts from sample III and then is propagated to sample II with snapping stresses at approximately 10 and 13 kPa, respectively. Experimental results of another $2 \times 2 \times 2$ shellular consisting of identical unit cells are presented in Figure S13 and Video S2, Supporting Information, showing indeterministic snapping sequence. In addition, the trend exhibited in Figure 2g is also validated by compression test on a $2 \times 1 \times 1$ shellular in Figure S14, Supporting Information.

Even though the assembly of bistable perforated shellular motifs can facilitate designing multistable structures, the number of stable configurations will be limited since each perforated P shellular motif possesses at most two stable states. Exploring perforation patterns that enable multistability of shellular motifs can pave the way for designing highly reconfigurable multifunctional metamaterials for shape-morphing applications. To realize multistable perforated shellulars, instead of adding multilayer circle or elliptical holes (see Figure S15, Supporting Information), we create multilayer staggered rectangular perforations on the shellular surface. Figure 3a shows perforation patterns on one-eighth of P shellular's mid-surface with f as 0.8, where the brown area represents a single staggered perforation layer (i.e., a hinge), characterized by projected layer height (δh), projected layer distance (δc), the projected height (t') of circumferential beam (purple part in top right inset), and radial beam (orange part in the top right inset) spacing angle α . Different from the previous compression—bending bistable mechanism in perforated shellulars (Figure 1a), the induced bistability of each staggered layer arises mainly from the counteraction between bending and torsion force of the flexible

circumferential beam of staggered perforation pattern. Due to the high rigidity of rings connecting the neighboring staggered layers, the generated torsion and bending cannot be transferred to the adjacent layers and structural instability is localized in one specific staggered layer at a time, leading to a layer-by-layer multistable behavior when multiple staggered perforations are created on the shellular surface. Since the bistability of each layer is decoupled from the rest of the layers, creating n -layer staggered perforations on the surface of P shellular motif can result in a maximum of 2^{n-1} stable states during loading and unloading. Owing to the narrow flexible regions in staggered perforations, P shellular surfaces with small level set constants are not preferred for multistable design. In this research, different combinations of t' and α , which determine the bending and torsion stiffness of the flexible circumferential beam, are analyzed through numerical simulation and experimentation on 3D printed samples. In specific, five different structures, that is, $t' = 0.5$ mm and $\alpha = 6^\circ$ (Sample M-I), $t' = 0.5$ mm and $\alpha = 18^\circ$ (sample M-II), $t' = 1$ mm and $\alpha = 10^\circ$ (sample M-III), $t' = 1.5$ mm and $\alpha = 6^\circ$ (sample M-IV), and $t' = 1.5$ mm and $\alpha = 18^\circ$ (sample M-V) are involved and each of them is 3D printed with three replicates. All these five samples include three perforation layers and share the same level set constant ($f = 0.8$), P shellular size ($2S = 50$ mm), shell thickness ($t = 1$ mm), layer height ($\delta h = 3$ mm), and layer distance ($\delta c = 4.5$ mm). Similar to the bistable shellular cell in Figure 1d, a solid frame with width of 10 mm and a solid cylinder bars with the height of 10 mm are used to constrain four sides, and top part of the staggered perforation motif, respectively.

As presented in Figure 3b, apart from the initial state, the half shellular with a three-layer staggered perforation would exhibit at most another three stable states. In addition, snap-back behavior is observed from the loading and unloading stress-strain curves, indicated by the sudden vertical changes in the stress instead of following the true path shown in dashed lines. It is noted that these dashed lines are inaccessible from conventional implicit dynamic analysis, and is determined through arc-length method and using shell elements for perforated shellulars (see Figures S16 and S17, Supporting Information). The bistable element of the multistable shellular with staggered perforation consists of flexible horizontal beam and a relatively rigid inclined plate (see Figure 3c). Upon high compressive strain, the counteraction between the downward bending and upward torsion reaction forces of the flexible beam leads to a new stable configuration. Therefore, flexible beam length, L_t , and width, W_t , are two key parameters for designing the multistable shellulars with staggered perforation.

Based on the proposed spring model and relationship between geometrical parameters and structural properties (Figure S18, Supporting information), the contour of normalized snapping force, F_{max} , with respect to flexible beam length, L_t , and width, W_t , is presented in Figure 3d. An increase of beam length and a decrease of beam its width contribute to a smaller snapping force and weakening the bistability, indicated by the monostable snap-through domain with combination of large L_t and small W_t and soft design region featured by small snapping force close to the boundary of bistable and snap-through domains. This is because of the inverse relation of the bending and torsional stiffnesses with L_t^2 and $1/W_t$, respectively.

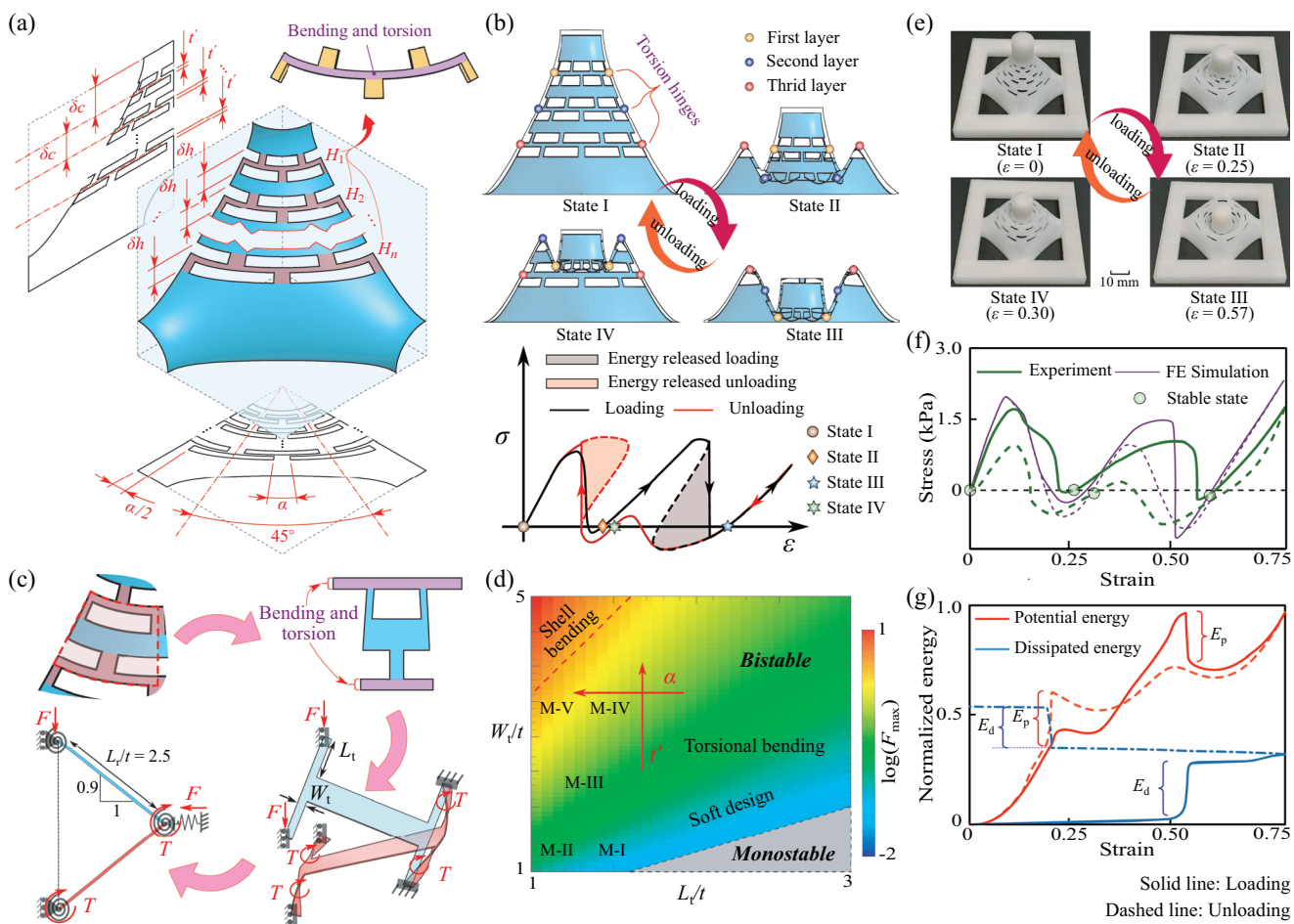


Figure 3. Multistable behavior of staggered perforated P shellulars. a) Schematic view showing the staggered perforated P shellular. b) Representative deformation pattern and stress–strain curve of the designed multistable metamaterial’s motif during the loading and unloading. c) Flexible bending–torsion-induced bistable element, representing the staggered perforation layer, and the corresponding simplified spring model consisting of compressive and torsional springs. d) Contour of normalized snapping force, F_{\max} , with respect to flexible beam length, L_t , and width, W_t . e) Four stable states of sample M-II sample during loading and unloading. f) Experimental and numerical simulation for stress–strain curve of 3D printed sample M-II. g) Potential and dissipation energy versus strain for sample M-II, obtained by simulation.

Accordingly, increasing beam length has dominant effect on decreasing bending stiffness, leading to monotonic snap-through behavior. Alternatively, since the bending stiffness is directly proportional to the cubic of the beam width opposed to the torsional stiffness that is directly proportional with beam width, decreasing the beam width drastically weaken the bending stiffness and impede the structural bistability. Therefore, sample M-V exhibits the strongest bistability, while sample M-I is in the vicinity of monostable snap-through domain.

Figure 3e shows four stable configurations of 3D printed sample M-II, including three noninitial stable states. In displacement-control experiment, the dashed lines presented in Figure 3b are inaccessible and two sudden drops in the stress–strain curve (at $\epsilon = 0.23$ and $\epsilon = 0.55$) are observed in Figure 3f due to the snap-back behavior. The close agreement between experimental and FE simulation results validates the accuracy of our numerical simulation and theoretical analysis. The sudden shape-changing caused by the snap-back instability of perforated shellulars leads to energy dissipation (E_p in Figure 3g) which is converted into kinetic energy and finally

thermal energy. The dissipated energy versus strain clearly demonstrates the snap-back induced energy dissipation (E_d in Figure 3g) that contributes to most of the damped energy during loading and unloading of these metamaterials and is desirable for developing reusable energy-absorbers.

To have a better understanding of the influence of geometrical parameters on the structural multistability, Figure 4a presents the number of stable configurations of the five 3D printed staggered perforated P shellular motifs. Increasing the circumferential angle α and decreasing the flexible beam height t' lead to the maximum number of stability, that is, 4 stable configurations found in sample M-II. In specific, sample M-I misses the stable state II in Figure 3b while sample M-II exhibits all the four representative stable states. For the remaining samples M-III, M-IV, and M-V with three stable states, the loading and unloading deformation patterns are symmetrical, where state IV in Figure 3b is replaced by stable state II during unloading (Figure S19 and S20, Supporting information). Video S3, Supporting Information, shows our experimentations on these samples under uniaxial loading and unloading tests.

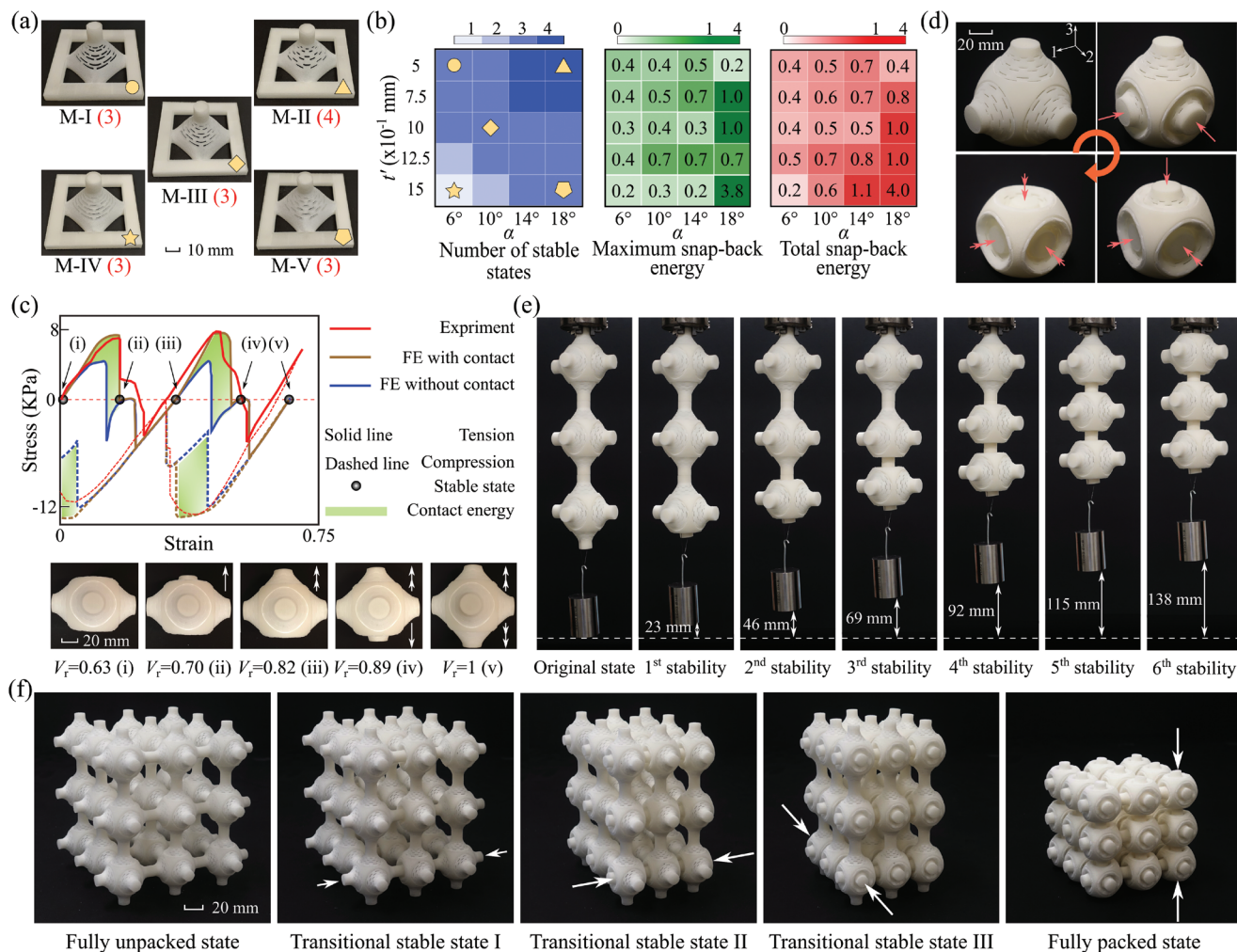


Figure 4. Analysis of geometrical parameters' effect on the snapping behavior of the designed multidirectional multistable perforated shellular metamaterials. a) Five 3D printed motifs. Red numbers in parenthesis indicate the number of stable states including the initial configuration, determined by experiment. b) Contour associated with the number of stable states (left grid in blue color), maximum snap-back induced energy dissipation (middle grid in green color), and total snap-back induced energy dissipation during a cyclic load (right grid in red color) with respect to the circumferential angle α and flexible beam height t' , determined by FE simulation. c) Experimental and FE simulation of stress–strain curve of initially packed multidirectional multistable perforated shellular unit cell under uniaxial tension and compression. Five stable states of the perforated shellular unit cell during tension are highlighted. d) 3D deployment of multidirectional multistable unit cell. e) Load bearability of an ensemble of $3 \times 1 \times 1$ cells of the designed multidirectional multistable perforated shellular material under tension at selected stable configurations when exploited to hold 1 kg weight. f) A multidirectional multistable $3 \times 3 \times 3$ perforated shellular metamaterial with fully packed, fully unpacked, and a selected number of intermediate transitional stable states.

A comprehensive parametric study on the multistable behavior of staggered perforated shellulars by FE simulation is conducted (Section S12, Supporting Information) and number of stable states (blue contour), maximum snap-back induced energy dissipation (green contour) during loading and unloading, and total snap-back induced energy dissipation during cyclic loading (hysteresis) (red contour), are presented in Figure 4b. It is noted that apart from sample M-IV, experimental observations on the number of stable configurations presented in Figure 4a for the other four 3D printed samples are in agreement with FE simulation predictions. The discrepancy between the number of stable states observed from experimental (3 stable states) and numerical anticipation (1 stable state) in sample M-IV is because the frictional forces arising

from the self-contact of the deformed shellular provide extra forces that hold the shellular at unanticipated stable states. However, the self-contact is not observed in the FE simulation, which might be due to the difference between the as-designed and SLS 3D printed as-built samples (Figure S21, Supporting information). To assess the snap-back induced energy dissipation, the maximum and total snap-back energy dissipations presented in Figure 4b are normalized by the corresponding values of a motif with $\alpha = 18^\circ$ and $t' = 1$ mm. Generally, both contours share similar trend as the snapping force in spring model (Figure 3d), where increasing α and t' results in higher dissipated snap-back energy dissipation and snapping force.

By tailoring the staggered perforation patterns along one direction, we have accomplished unidirectional multistability

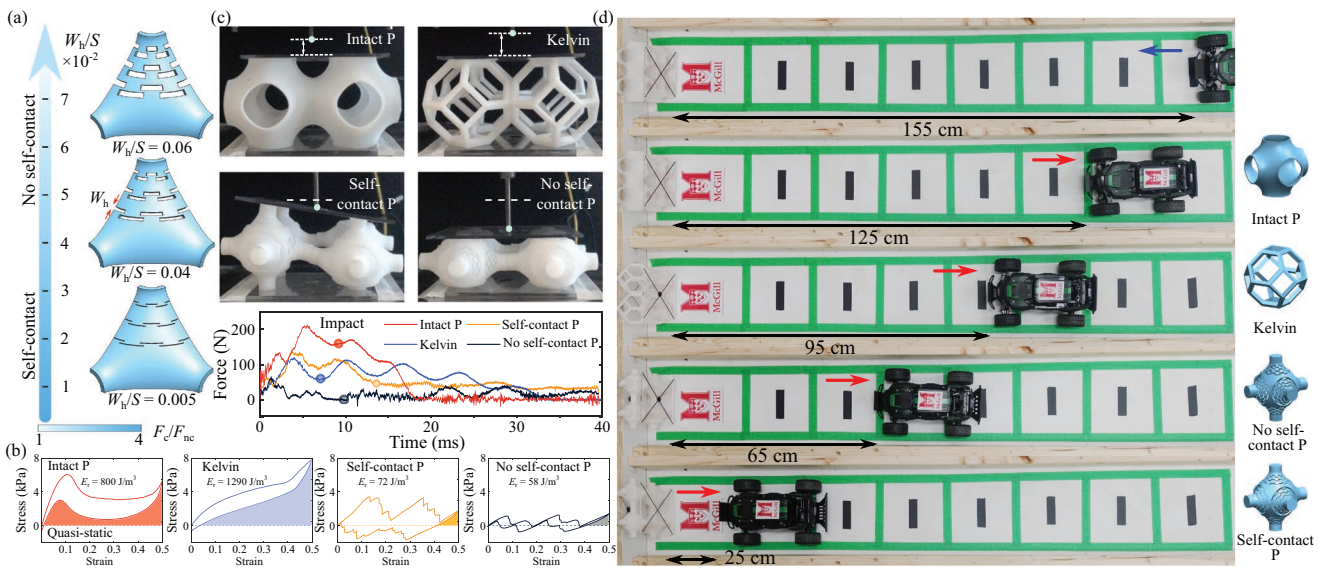


Figure 5. Energy absorption traits of multistable perforated P shellular metamaterials under quasi-static and low-velocity impact tests. a) Influence of perforation width on the self-contact mechanism of multilayer perforated P shellular. b) Quasi-static compression-tension test on $2 \times 2 \times 1$ intact P shellular, Kelvin, no self-contact P shellular, and self-contact P shellular materials. c) Low-velocity impact test by dropping a 917.8 g mass from 81 mm height. The pictures are captured from the Supporting Video (Video S5, Supporting Information) and show the maximum rebound height for intact P shellular and Kelvin cell materials. d) Damping performance of four materials when impacted by a moving electric car; blue and red arrows present the direction of forward (before impact) and rebound (after impact) motions.

in perforated shellular metamaterials' motifs. Since intact P shellulars have mutually independent flexible regions in three orthogonal orientations, one stimulating question is whether we can realize multidirectional multistability in perforated P shellulars by patterning the shell surface with staggered perforations aligned with all three directions. Here, the perforation pattern introduced in Figure 3a is designed in all six regions of P shellulars along the $\pm x$, $\pm y$ and $\pm z$ directions. In addition, in order to achieve multidirectional multistability, the solid frame in Figure 4a is removed and instead, the shell region without any perforation between the six motifs is further stiffened (Figure S1e, Supporting information). To corroborate the validity of this multidirectional multistable design, Figure 4c initially shows its stress-strain curves under uniaxial tension and compression tests. During tension, besides the initial state (i), four other stable states are observed, twice of the stable states found in the unidirectionally multistable half-unit cell, and approve the multistability of the designed multidirectional perforated shellular. In specific, as presented in the stable configurations, the upper two perforation layers first switch to two stable states followed by the shape-changing of bottom two layers. Shape morphing of multidirectional multistable perforated shellular leads to noticeable volume change (relative volume V_r varies from 0.63 for state (i) to 1 for state (v)). Opposed to tension, during compression, only part of the unit cell restore to its original state and further deformation is needed to ensure the full recoverability of the multidirectional shellulars (Figure S22, Supporting information). It is noted that self-contact is observed during the cyclic tension-compression; this behavior is considered in FE simulation by assigning a frictional factor to the constitutive solid material. The good agreement between experimental and FE (with contact) results proves the accuracy of our numerical model.

Apart from the snap-back induced energy dissipation, the self-contact behavior imparts a new mechanism to lock the deformed cell in stable configurations and enhance the snapping force required for triggering new stable states, and to dissipate a higher level of energy, that is, enclosed by two FE (with and without contact) curves. The shape morphing of the multidirectional multistable perforated shellular unit cell, with possible applications as a building block for developing soft and load-bearable robotic muscles or constructing impact energy absorbers, is presented in Figure 4d. The perforated motifs of this unit cell along the three orthogonal directions can be independently transformed into up to four stable configurations during tension and compression. The 3D printed shellular in Figure 4d presents about 75% reduction in the volume of unit cell when is morphed from the initial to the most compact stable state. Figure 4e demonstrates the load bearability of a multistable perforated shellular metamaterial comprised of $3 \times 1 \times 1$ unit cells at seven representative stable configurations at which 1 kg weight is added at the bottom of the shellular metamaterial, that remains at stable states under the applied tensile load. To further corroborate that our designed perforated shellular unit cell can be tessellated in three directions and be used to construct materials, Figure 4f presents five representative stable states of a 3D printed $3 \times 3 \times 3$ perforated shellular metamaterial. The multistability along the three directions still can be realized in each direction, decoupled from the others, after tessellation of unit cells. The fully packed stable state demonstrates close to 25% of the volume of the fully unpacked one.

In order to study the absorbed/dissipated and stored energy properties of multistable perforated P shellular materials, Figure 5 demonstrates their performance under quasi-static and impact tests. Figure 5a presents a relationship between the non-dimensional perforation width (W_h/S)

and perforation-induced self-contact, quantified by the ratio of numerical reaction force F_c (when surface penetration is restricted during loading/unloading—self-contact) and F_{nc} (when surface penetration is allowed—no self-contact). The lower the perforation width, the higher the reaction force ratio, which leads to enhanced energy dissipation and increased maximum reaction force applied by multilayer perforated P shellular to the loading nose or impactor. A comprehensive parametric study on the effect of architectural features of perforation on the self-contact occurrence and the associated stress-strain curves can be found in Figure S23, Supporting information.

Figure 5b presents the quasi-static loading (compression) and unloading (tension) stress–strain curves of $2 \times 2 \times 1$ self-contact ($W_h/S = 0.04$) and no self-contact ($W_h/S = 0.06$) multilayer perforated P shellular materials. Intact P shellular ($f = 0$) and Kelvin cell-based materials with 0.04 relative density and $160 \times 160 \times 80$ mm dimension, the same as the corresponding values for multilayer shellular samples, are considered for the sake of material performance comparison. Multilayer staggered perforations convert the stiff monostable intact P shellular to a less stiff multistable perforated P shellular. The shell surface contact in the self-contact multilayer perforated P shellular materials enhances the reduced stiffness and strength and improves energy absorption and dissipation. In contrast to the other samples, Kelvin-based cellular materials present a monotonous stress–strain curve. The area under the stress–strain curve in loading determines absorbed energy by material, while the enclosed area between the loading and unloading curves identifies dissipation energy. The shaded area below the unloading curve, till the nearest stable configuration, indicates the returned energy density E_r , which is released to the system upon removal of the external load. After applying 0.5 compressive strain and removing the external load, compared to intact P shellular ($E_r = 800 \text{ J m}^{-3}$) and Kelvin ($E_r = 1290 \text{ J m}^{-3}$), most of the absorbed energy is trapped inside the multistable perforated shellulars, leading to a lower returned energy $E_r = 72$ and 58 J m^{-3} for perforated shellular with and without self-contact, respectively. The reduced returned energy plays an important role in developing dampers (e.g., helmet and car bumper) that safely protect human or goods against impact. The test process is recorded in Video S4, Supporting Information.

Figure 5c shows the drop weight impact test results on the abovementioned 3D printed samples, sandwiched between two plexiglass sheets and impacted by a 917.8 g mass dropped from 81 mm height (0.73 J impact energy). Intact P shellular materials show the highest impact peak force, while no self-contact P shellular metamaterials impose the lowest impact force (around 200 N and 50 N, respectively). The shell surface contact in the self-contact P shellular metamaterial increases the impact force to 120 N, close to the 3D printed Kelvin sample. Due to the higher returned energy, after impact on the intact P shellular and Kelvin samples, the impactor rebounds significantly, opposed to the multistable multilayer perforated shellular metamaterials that stop the impactor immediately after the impact phenomenon. More information can be found in Figure S24 and Video S5, Supporting information. We also conduct a remote control (RC) car impact test on these materials where the car starts to move from a 155 cm distance prior to the collision to the 3D printed dampers. As illustrated in

Figure 5d, after the impact, the electric car rebounds backward freely and finally stops at distances (e.g., 125 cm for intact P shellular and 25 cm for self-contact perforated P shellular metamaterials) depending on the returned energy of the cellular/shellular materials. More details about this test can be found in Figure S25 and Video S6, Supporting information.

3. Conclusion

We have developed a novel class of P shellular metamaterial, which can be one/two/three-directional multistable, deployable, programmable, and reusable under both tension and compression, enabled by a delicate and systematic design of the perforation patterns. The designed reconfigurable metamaterials also share the unique traits of shellular materials, such as high surface area, stiffness, and energy absorption. Two perforation design strategies are introduced and the associated mechanical and stability properties of the perforated shellulars are analyzed by theoretical mechanics models, FE simulations, and mechanical testing on SLS 3D printed samples. The first strategy realizes bistable shellular motifs by introducing elliptical holes where the bistability arises from the balance between compression-induced buckling and bending of flexible parts. The mechanical responses of these perforated shellular structures can be controlled by tuning the geometrical parameters of the underlying shell and their perforation, while the deformation sequence of their stacked assembly can be programmed by tuning the snapping force of each shellular layer. In the second strategy, a multistable shellular motif is developed via multilayer staggered perforations. The bending-torsional hinges, imparted by staggered perforations in each layer, contribute to the overall multistability of perforated shellular metamaterials. With n -layer staggered perforations (n hinges), maximum 2^{n-1} stable states can be achieved in each shellular motif, offering a new paradigm for realization of desired number of stable configurations in shell-like mechanical metamaterials. Using rationally designed multistable motifs with staggered perforation, we have demonstrated how multidirectional multistable shellulars with load-bearing stable configurations can be attained. Compared to the existing bistable metamaterials, our developed and prototyped multistable metamaterials are based on multistable perforated shellular motifs (rather than bistable truss motifs), and damp energy through a combined snap-back and self-contact induced energy dissipation mechanisms. Experiments confirm the load-bearing ability of multiple stable states of perforated P shellulars under tension and compression, while low-velocity drop weight impact tests and RC car collision tryouts corroborate their programmable energy damping performance. We deem the designed perforated shellular metamaterials capable of serving as a next generation of multifunctional metamaterials with versatile applications, spanning from the reusable energy absorbers/dampers and programmable wave filters to reconfigurable and intelligent robotic arms and microelectromechanical systems.

Supporting Information

Supporting Information is available from the Wiley Online Library or from the author.

Acknowledgements

J.S., H.M., and A.M. contributed equally to this work. A.H.A. acknowledges the financial support by Natural Sciences and Engineering Research Council of Canada through NSERC Collaborative Research and Development Grants (CRDPJ 543334-19). This research was undertaken, in part, thanks to funding to A.H.A. from the Canada Research Chairs program in Multifunctional metamaterials. J.S. acknowledges the financial support provided by the China Scholarship Council (File No. 201706220086) and McGill University. Authors acknowledge the contributions of Thomas Fauquet at Axis Prototypes Inc. for SLS 3D printing of perforated shellulars, and Daniel Poirier and Mathieu Lapointe at Composites Development Center of Quebec (CDCQ) for conducting impact tests.

Note: The figures were reset in higher resolution on October 21, 2021, after initial publication online. Text that had been included in Figure 1h in error was also removed. In addition, some corrections were made with regard to the presentation of 2^{n-1} in the pdf version on pages 6 and 10 and in the abstract and table of contents text. Some minor typos on page 2 and 10 were also corrected.

Conflict of Interest

The authors declare no conflict of interest.

Data Availability Statement

Research data are not shared.

Keywords

mechanical metamaterials, multidirectional multistability, P shellular, programmable properties, staggered perforation

Received: March 29, 2021

Revised: June 30, 2021

Published online: August 31, 2021

- [1] V. M. Shalaev, W. Cai, U. K. Chettiar, H.-K. Yuan, A. K. Sarychev, V. P. Drachev, A. V. Kildishev, *Opt. Lett.* **2005**, *30*, 3356.
- [2] V. M. Shalaev, *Nat. Photonics* **2007**, *1*, 41.
- [3] A. Rafsanjani, A. H. Akbarzadeh, D. Pasini, *Adv. Mater.* **2015**, *27*, 5931.
- [4] T. A. M. Hewage, K. L. Alderson, A. Alderson, F. Scarpa, *Adv. Mater.* **2016**, *28*, 10323.
- [5] K. Bertoldi, P. M. Reis, S. Willshaw, T. Mullin, *Adv. Mater.* **2010**, *22*, 361.
- [6] C. Z. Fan, Y. Gao, J. P. Huang, *Appl. Phys. Lett.* **2008**, *92*, 251907.
- [7] K. Bertoldi, M. C. Boyce, *Phys. Rev. B* **2008**, *77*, 52105.
- [8] P. Wang, F. Casadei, S. Shan, J. C. Weaver, K. Bertoldi, *Phys. Rev. Lett.* **2014**, *113*, 14301.
- [9] J. Y. Ou, E. Plum, L. Jiang, N. I. Zheludev, *Nano Lett.* **2011**, *11*, 2142.
- [10] N. I. Zheludev, E. Plum, *Nat. Nanotechnol.* **2016**, *11*, 16.
- [11] S. Shan, S. H. Kang, J. R. Raney, P. Wang, L. Fang, F. Candido, J. A. Lewis, K. Bertoldi, *Adv. Mater.* **2015**, *27*, 4296.
- [12] B. Haghpanah, L. Salari-Sharif, P. Pourrajab, J. Hopkins, L. Valdevit, *Adv. Mater.* **2016**, *28*, 7915.
- [13] X. Xia, A. Afshar, H. Yang, C. M. Portela, D. M. Kochmann, C. V. Di Leo, J. R. Greer, *Nature* **2019**, *573*, 205.
- [14] F. Pan, Y. Li, Z. Li, J. Yang, B. Liu, Y. Chen, *Adv. Mater.* **2019**, *31*, 1900548.
- [15] B. Haghpanah, A. Shirazi, L. Salari-Sharif, A. Guell Izard, L. Valdevit, *Extrem. Mech. Lett.* **2017**, *17*, 56.
- [16] X. Tan, B. Wang, K. Yao, S. Zhu, S. Chen, P. Xu, L. Wang, Y. Sun, *Int. J. Mech. Sci.* **2019**, *164*, 105168.
- [17] T. Chen, O. R. Bilal, K. Shea, C. Daraio, *Proc. Natl. Acad. Sci. USA* **2018**, *115*, 5698.
- [18] H. Shao, S. Wei, X. Jiang, D. P. Holmes, T. K. Ghosh, *Adv. Funct. Mater.* **2018**, *28*, 1802999.
- [19] Y. Jiang, L. M. Korpas, J. R. Raney, *Nat. Commun.* **2019**, *10*, 128.
- [20] J. Qiu, J. H. Lang, A. H. Slocum, *J. Microelectromech. Syst.* **2004**, *13*, 137.
- [21] M. Alturki, R. Burgueño, *Thin-Walled Struct.* **2019**, *140*, 74.
- [22] J. R. Raney, N. Nadkarni, C. Daraio, D. M. Kochmann, J. A. Lewis, K. Bertoldi, *Proc. Natl. Acad. Sci. USA* **2016**, *113*, 9722.
- [23] H. Yang, L. Ma, *Mater. Des.* **2020**, *188*, 108430.
- [24] J. Hua, H. Lei, Z. Zhang, C. Gao, D. Fang, *J. Appl. Mech.* **2019**, *86*, 071007.
- [25] J. Meaud, K. Che, *Int. J. Solids Struct.* **2017**, *122–123*, 69.
- [26] H. Y. Jeong, E. Lee, S. Ha, N. Kim, Y. C. Jun, *Adv. Mater. Technol.* **2019**, *4*, 1800495.
- [27] H. Fang, K. W. Wang, S. Li, *Extrem. Mech. Lett.* **2017**, *17*, 7.
- [28] S. Zhu, X. Tan, B. Wang, S. Chen, J. Hu, L. Ma, L. Wu, *Extrem. Mech. Lett.* **2019**, *32*, 100548.
- [29] X. Tan, S. Chen, B. Wang, S. Zhu, L. Wu, Y. Sun, *Extrem. Mech. Lett.* **2019**, *28*, 8.
- [30] K. Fu, Z. Zhao, L. Jin, *Adv. Funct. Mater.* **2019**, *29*, 1901258.
- [31] M. Pezzulla, N. Stoop, M. P. Steranka, A. J. Bade, D. P. Holmes, *Phys. Rev. Lett.* **2018**, *120*, 48002.
- [32] M. Taffetani, X. Jiang, D. P. Holmes, D. Vella, *Proc. R. Soc. A* **2018**, *474*, 20170910.
- [33] Y. Forterre, J. M. Skotheim, J. Dumais, L. Mahadevan, *Nature* **2005**, *433*, 421.
- [34] P. M. Sobota, K. A. Seffen, *R. Soc. Open Sci.* **2020**, *6*, 190888.
- [35] A. D. Norman, K. A. Seffen, S. D. Guest, *Proc. R. Soc. A* **2008**, *464*, 1653.
- [36] A. Iniguez-Rabago, Y. Li, J. T. B. Overvelde, *Nat. Commun.* **2019**, *10*, 5577.
- [37] S. C. Han, J. W. Lee, K. Kang, *Adv. Mater.* **2015**, *27*, 5506.
- [38] S. C. Han, K. Kang, *Mater. Today* **2019**, *31*, 31.
- [39] H. Kashani, Y. Ito, J. Han, P. Liu, M. Chen, *Sci. Adv.* **2019**, *5*, eaat6951.
- [40] C. M. Portela, A. Vidyasagar, S. Krödel, T. Weissenbach, D. W. Yee, J. R. Greer, D. M. Kochmann, *Proc. Natl. Acad. Sci. USA* **2020**, *117*, 5686.
- [41] S. Hyde, B. W. Ninham, S. Andersson, K. Larsson, T. Landh, Z. Blum, S. Lidin, *The Language of Shape*, Elsevier Science B.V., Amsterdam, The Netherlands **1997**, pp. 1–42.
- [42] J. Shi, L. Zhu, L. Li, Z. Li, J. Yang, X. Wang, *Sci. Rep.* **2018**, *8*, 7395.
- [43] S. Tan, J. Gu, S. C. Han, D.-W. Lee, K. Kang, *Mater. Des.* **2018**, *142*, 229.
- [44] M. S. Morey, A. Davidson, G. D. Stucky, *J. Porous Mater.* **1998**, *5*, 195.
- [45] T. Femmer, A. J. C. Kuehne, M. Wessling, *Chem. Eng. J.* **2015**, *273*, 438.
- [46] N. Sreedhar, N. Thomas, O. Al-Ketan, R. Rowshan, H. Hernandez, R. K. Abu Al-Rub, H. A. Arafat, *Desalination* **2018**, *425*, 12.
- [47] J. G. Werner, G. G. Rodríguez-Calero, H. D. Abrúñia, U. Wiesner, *Energy Environ. Sci.* **2018**, *11*, 1261.
- [48] R. Sachse, A. Westermeier, M. Mylo, J. Nadasdi, M. Bischoff, T. Speck, S. Poppinga, *Proc. Natl. Acad. Sci. USA* **2020**, *117*, 16035.
- [49] H. G. von Schnering, R. Nesper, *Zeitschrift für Phys. B Condens. Matter* **1991**, *83*, 407.
- [50] O. R. Bilal, A. Foehr, C. Daraio, *Proc. Natl. Acad. Sci. USA* **2017**, *114*, 4603.